Int J Earth Sci (Geol Rundsch) (2016) 105:2311–2326
DOI 10.1007/s00531-015-1289-5

ORIGINAL PAPER

3D seismic interpretation of subsurface eruptive centers in a Permian large igneous province, Tazhong Uplift, central Tarim Basin, NW China

Jiangfeng Yang[1,2] · Wenbin Zhu[1] · Da Guan[2] · Beibei Zhu[2] · Liansheng Yuan[2] · Xuemei Xiang[2] · Jinbao Su[3] · Jingwen He[1] · Xinhui Wu[4]

Received: 29 April 2015 / Accepted: 15 December 2015 / Published online: 29 December 2015

Abstract A 1445-km^2 high-resolution 3D seismic reflection dataset is used to analyze the Permian large igneous province in the subsurface of the Tazhong area in the central Tarim Basin in northwestern China. Constrained by the synthetic seismograms of four wells, the top and base of the igneous rocks were identified in the seismic data. Seven large volcanic craters, each >10 km^2 in area, have been discovered via the application of coherency and amplitude attributes. The thickness and volume of the igneous rocks were obtained by time–depth transformation. In the study area, all of the igneous rocks, with thicknesses from 120 to 1133 m, were formed by eruptions in the Early Permian. These events produced huge erupted volumes (178 km^3) and multiple closely spaced volcanic edifices (<13 km). These features suggest that the study area may be the part of the eruptive center of the Permian igneous rocks in the Tarim Basin.

Keywords Tarim · Permian · Large igneous province · 3D seismic · Eruptive center

✉ Wenbin Zhu
zwb@nju.edu.cn

[1] State Key Laboratory for Mineral Deposits Research, Department of Earth Sciences, Nanjing University, Nanjing 210093, Jiangsu, China

[2] SINOPEC Geophysical Research Institute, Nanjing 211103, Jiangsu, China

[3] School of Earth Sciences and Engineering, Hohai University, Nanjing 210098, Jiangsu, China

[4] Institute for Computational and Mathematical Engineering, Stanford University, Stanford 94305, CA, USA

Introduction

Lower-Middle Permian magmatic rocks are widely distributed in the Tarim Basin and cover an area of ~250,000 km^2. The rocks are primarily basalt and diabase, with some basaltic andesite. Most of the igneous rocks are overlain by younger sedimentary strata (Yang et al. 1996, 1997; Chen et al. 1997a, b; Jia 1997; Liu et al. 2011; Shangguan et al. 2012). With the development of the mantle plume theory and the confirmation of the existence of the Emeishan large igneous province (Ali et al. 2005; Xu et al. 2004, 2007; Zheng et al. 2010), the Permian igneous rocks in the Tarim Basin have received significant attention in recent years. Chronological data (Yang et al. 2006a, b; Zhang et al. 2008; Chen et al. 2010a) indicate that the major eruptive episode occurred in the Early Permian. Yu et al. (2011) have constrained the duration of the entire eruption to no more than 5.5 Ma using SHRIMP U–Pb zircon dating. Geochemical analyses demonstrate that the Tarim Basin's Permian igneous rocks exhibit ocean island basalt (OIB)-like characteristics and negative εNd values, which are consistent with a mantle plume origin (Chen et al. 1997a, b; Yang et al. 2005; Tian et al. 2010b; Yu et al. 2011; Zhang et al. 2008, 2012; Shangguan et al. 2012; Li et al. 2012a, b). Therefore, a possible Permian large igneous province with a mantle plume origin in the Tarim Basin has been proposed by previous workers (Zhang et al. 2008, 2012, 2013; Zhang and Zou 2013). The igneous rocks including basalt, diabase and basaltic andesite in the Tarim Basin may be resulted from plume–lithosphere interactions (Yang et al. 1997; Zhang et al. 2008, 2010a, b, 2012, 2013; Zhang and Zou 2012, 2013; Zhou et al. 2004, 2009; Pirajno et al. 2009; Tian et al. 2010a; Zhang et al. 2010c; Li et al. 2011, 2012a, b).

Constrained by the Taklamakan Desert surface in the central Tarim Basin, previous studies have primarily used

samples from outcrops along the margins of the basin and from cores from several wells, and these studies have predominantly focused on certain rock types, such as flood basalts, acid lava and intrusive rocks (Yang et al. 2007; Zhang et al. 2008; Zhang and Zou 2012, 2013). Studies of the internal parts of the basin are rare. In recent years, seismic data have been applied to distinguish the subsurface volcanic rocks (Davies et al. 2002; Zhang 2003; Brown 2004; Wang et al. 2006; Wagner-Friedrichs et al. 2008; Chen et al. 2009; Li et al. 2009; Sun et al. 2010; Liu et al. 2011; Wright et al. 2012; Xu et al. 2012; Magee et al. 2013a, b; Schofield and Jolley 2013), and these techniques highlight a new direction for the study of the igneous rocks underlying the thick sedimentary deposits. Zhang (2003) predicted the occurrence of igneous rocks by applying seismic techniques (including seismic modeling, impedance inversion and seismic attribute analysis) to 2D seismic reflection data from the Tazhong area. Wang et al. (2006) used coherency analysis to map the distribution of local igneous rocks in the Tazhong area using 326 km^2 of 3D seismic data. Liu et al. (2011) integrated 2D seismic and drilling information to further study the residual area of Permian basalts in the Tarim Basin and estimated the area to be ~246,000 km^2. However, the precision of the predictions in these studies was severely restricted by poor data quality and the small areas covered by the seismic data.

The present paper uses 1445 km^2 of high-resolution 3D seismic reflection data and information from four wells to study the igneous rocks in the Tazhong area. Integrating geological and geophysical methods, we analyzed in detail the features of the Permian igneous rocks.

Geological setting

The Tarim Craton is one of the three major cratons in China, occupying an area of over 600,000 km^2, and is located to the southwest of the Central Asian Orogenic Belt, NW China (Fig. 1a). The craton is surrounded by the Tianshan Mountains to the north, the Altyn Mountains to the southeast and the West Kunlun Mountains to the southwest (Fig. 1b) and has a typical two-layered structure consisting of a crystalline basement and sedimentary cover. Most of the craton is covered by thick Mesozoic and Cenozoic sediments (Shu et al. 2011). Precambrian–Paleozoic rocks crop out primarily along the edge of the Tarim Basin in Kuruktag, Aksu, West Kunlun and the Altyn-Tagh–Dunhuang belt (Fig. 1b; Lu et al. 2008a, b; Ge et al. 2012). Permian basalts are widely distributed over an area of at least 250,000 km^2 and are found in areas in Keping, Bachu, Tabei (northern Tarim Basin), Tazhong (central Tarim Basin) and Taxinan (southwestern Tarim Basin) (Fig. 1b; Yang et al. 2005; Chen et al. 2006). This widespread distribution suggests the existence of a Permian large igneous province (Yang et al. 2007). The rocks are dominated by basalt, andesitic basalt, diabase and ultramafic units. Felsic series are also present and include syenite, rhyolite, dacite, granodiorite and pyroclastic rocks (Yu et al. 2011; Zhang and Zou 2012).

The Tazhong Uplift zone (Fig. 1b), one of the most important oil and gas accumulation zones in the Tarim Basin (Kang and Kang 1996; Lu et al. 2008a, b; Zhou et al. 2010; Du et al. 2011; Xiao et al. 2000), is located in the middle of the Tarim Basin and is bounded by the Northern Depression to the north, the Southwestern Depression to the south and the Bachu Uplift to the west (Wang et al. 2009). This NW–SE-trending uplift is 250–300 km long and approximately 100 km wide and covers an area of ~51,000 km^2. Early Paleozoic strata in the Tazhong Uplift form a broad anticline, and overlying younger Paleozoic formations dip toward the west to form a 'nose-shaped' structure. The Mesozoic and Cenozoic strata feature gentle dips, suggesting an inherited paleo-uplift from the long development history of the Tazhong uplift (Xiao et al. 2000; He et al. 2005; Zhang et al. 2003).

The research area is situated in the western part of the Tazhong Uplift. The Tazhong II fault zone (Cambrian–Early Ordovician) passes across the area's southern portion (Fig. 1c), and small NNE-trending faults associated with Permian magmatic plugs are also present in the region (Li et al. 2013). Except for a hiatus which spans the entire Jurassic, sedimentary formations from Cambrian to Quaternary systems are developed in the study area (Fig. 2) and approach a total thickness of 10,000 m. The Cambrian series consists of a succession of gray to dark gray limestone and dolomite with gypsum and salt layers, which are characteristic of an evaporative carbonate platform environment. The Ordovician carbonate system is predominantly composed of thick limestones and dolomites associated with an open platform. An unconformity exists between the Lower-Middle and Upper Ordovician. The Silurian and Devonian series are primarily sandstone and mudstone interbedded with tidal-flat sediments. The contact between the Silurian and Ordovician series is an angular unconformity. The Carboniferous series is primarily sandstone and limestone with intercalated mudstone. The Permian series consists of sandstone, mudstone and volcanic rocks. The volcanic rocks are primarily observed in the Early Permian Kupukuziman and Kaipaizileike Formations, which are dominated by basalts and tuffs separated by layers of sandstone. The overlying strata above the Permian are primarily detrital rocks (Fig. 2).

Following the nomenclature used in the field of oil exploration, we named the seismic reflection layers as follows: T40, the reflection interface of the lower boundary of the Cretaceous; T50, the lower boundary of the Triassic; T51, the upper boundary of the Kaipaizileike; T52, the

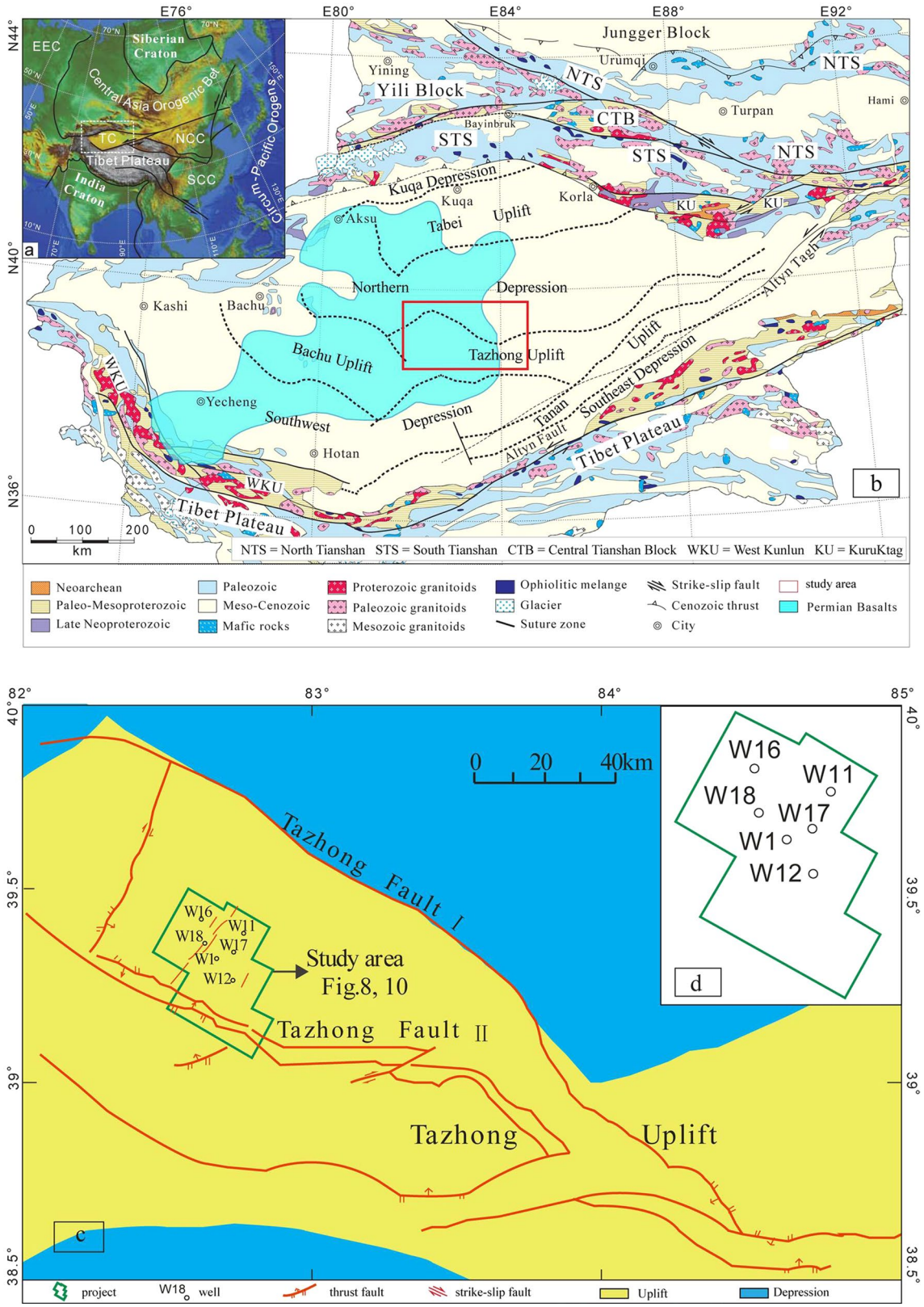

Fig. 1 **a** Topographic map of Asia showing the main tectonic units and the location of the Tarim Craton (TC); *NCC* North China Craton, *SCC* South China Craton, *EEC* East European Craton. **b** Geotectonic map of Tarim and adjacent terrains showing the distribution of the Permian basalts (*light blue shading*). The distribution of Permian basalts is after Yang et al. (2007). The *red box* is the location of (**c**). **c** Geological sketch map of the study area; the *yellow shading* indicates the area of tectonic uplift, and the *blue shading* indicates the area of tectonic depression. The *green box* is the 3D work area. **d** Close-up of the well location

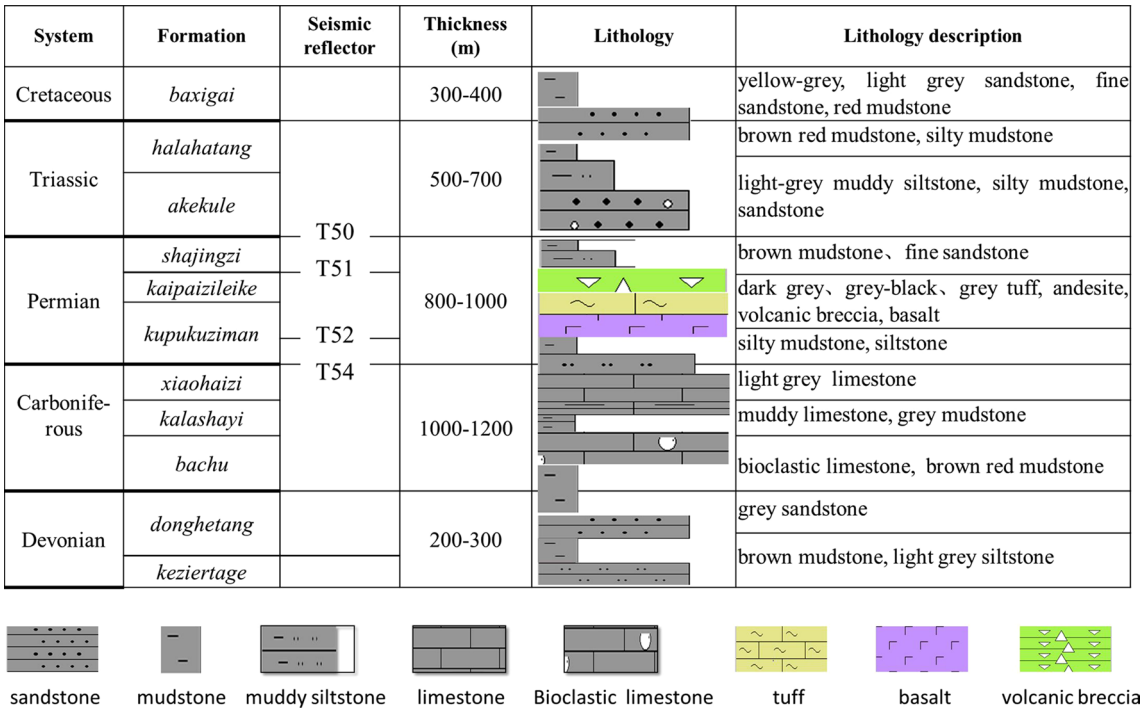

Fig. 2 Composite stratigraphic column of the Tazhong area. T50—bottom surface reflection of Triassic strata; T51—top surface reflection of the Kaipaizileike formation in Permian; T52—bottom surface reflection of the Kupukuziman formation volcanic rock in the Permian; T54—bottom surface reflection of Permian strata

lower boundary of the igneous rocks in the Kupukuziman; T54, the lower boundary of the Permian; T57, the lower boundary of the Carboniferous and the Bachu Formation; T70, the lower boundary of the Silurian; T80, the lower boundary of the Ordovician; and T81, the lower boundary of the Upper Cambrian (Fig. 2).

Data and methodology

The 3D seismic data have a recording length of 8 s TWT (two-way travel time) and a bin size of 25 m × 25 m. After zero-phase pre-stack time migration, the dominant frequency of the reflections generated by the Permian formations is ~30 Hz.

The four wells, originally deployed for petroleum exploration, end in the Ordovician formations. The logging data from these wells include acoustic (AC), density (DEN), deep investigative double lateral resistivity (RD) and shallow investigative double lateral resistivity (RS).

Identifying the lithology of an igneous rock via logging data is already a well-established technique (Sanyal and Mathews 1979; Benoit et al. 1980). Pan et al. (2008) described igneous rocks from the North Tarim Basin using core analysis and thin section identification; and Yang et al. (2013) made a lithologic identification model of Tazhong's igneous rocks based on 245 volcanic rock samples from well 10 in Tazhong. Combining the models from Pan et al. (2008) and Yang et al. (2013), we corrected the mud log cutting descriptions of wells w11, w12, w17 and w16 using GR, DEN, AC and RD logs.

The synthetic seismogram calibration and horizon interpretation were performed using the Landmark interpretation software. A 30-Hz Ricker wavelet was adopted to construct synthetic seismograms for the four wells. The Carboniferous Bachu Formation (T57) was used as a marker in the calibration because it is widely distributed across the Tarim Basin and has an almost constant thickness and parallel reflection pattern.

The TDQ module in the Landmark software was applied for time–depth conversion. Based on the synthetic seismogram calibration results of the four wells, the TDQ module generated time–depth tables that were then interpolated using triangulation methods to construct the time–depth volume. The time–depth volume can be used for conversion from time to depth or vice versa, and therefore, the corresponding depth of any surface can be extracted.

The volume of the igneous rock was computed using Petrel software. The structural model was constructed using the horizons in the depth domain. The grid size in this model is 25 m × 25 m (horizontal) × 10 m (vertical).

The seismic amplitude and coherency attributes were extracted to help identify the igneous rocks (Zhao et al. 2008). For the coherency analysis, a third-generation high-precision coherency algorithm was adopted to better discriminate igneous rocks from sedimentary rocks. This method, based on the eigenvalues of a covariance matrix, compares multiple traces, estimates similarities and performs strata-based dip and azimuth calculations. Given an estimate of the maximum true dip based on the seismic data, the range of the apparent dip pairs can be defined. The output coherency volumes can indicate the boundaries of formations, folds and rock masses; thus, they can be used to help recognize specific geological bodies. This method offers the advantages of strong anti-noise capabilities and high resolution (Gersztenkorna and Marfurtk 1999).

Results

In this study, firstly we determined the different igneous rock types ("Lithology" section); secondly, we determined the seismic patterns that characterize igneous rocks using the well-seismic ties ("Well-seismic calibration" and "Seismic recognition of igneous rocks" sections); thirdly, we described the spatial distribution characterization of igneous rocks using amplitude and coherency attributes ("Planar distribution of volcanic rocks" section); and finally, we calculated the thickness and volume of the igneous rocks ("Thickness and volume of the igneous rocks" section).

Lithology

The igneous rocks in the study area are dominated by dark gray and ash-black basalt, andesitic basalt, andesite, volcanic breccia and tuff and are interbedded with dark gray mudstone and silty mudstone. Among the igneous rock types, tuff and basalt are the most common (Zhu et al. 2005; Chang et al. 2003; Yan et al. 2014; Yang et al. 2013; Pan et al. 2008).

Compared with the Permian clastic rocks, the volcanic rocks are characterized by low gamma, high resistivity, high density and low acoustic values (Fig. 3; Table 1). The tuff exhibits low GR, relatively high DEN, medium–high AC and relatively high RD values; the basalt exhibits low GR and AC values, and high DEN and RD values; the andesite exhibits low–medium GR, low AC, and high DEN and RD values; and the volcanic breccia exhibits low GR and AC values, high DEN values and relatively higher RD values (see Table 1 for the exact values). Among the four lithologies, the features of the basalt are the most distinct: The GR results exhibit a box-shaped pattern with microgears, whereas the resistivity curves exhibit a peak-shaped or tooth-shaped pattern with large-amplitude variations. The andesite GR values are higher than those of the basalts, but the RD values are lower. The RD values of the volcanic breccia and tuff are significantly lower than those of the basalt and andesite. The volcanic breccia and tuff differ primarily in density: The volcanic breccia is slightly less dense than the tuff (Figs. 3, 5, 6).

Based on the positions of the volcanic rocks, their lithologies and seismic refection characteristics and the volcanic lithofacies classification schemes of Li and Wang (1980) and Wang et al. (2003), we divided the igneous rocks into five facies: volcanic vent facies, sub-volcanic facies, volcanic eruption facies, overflow facies and volcanogenic sedimentary facies. The characteristics of the five lithofacies are described in "Seismic recognition of igneous rocks" section.

Well-seismic calibration

Synthetic seismogram calibration links seismic and drilling data. In this study, a 30-Hz Ricker wavelet was adopted to perform well-seismic calibration. The results of the calibration showed that the upper surface of the Permian igneous rocks generates a continuous peak reflection (T51) with a medium–high amplitude. The bottom surface of the igneous rocks generates a continuous trough reflection with a high amplitude (T52). The base of the Permian strata corresponds to a continuous and stable peak reflection (T54), which is also of medium or high amplitude. The reflection features of the other interfaces are shown in Fig. 4.

Subtle characteristics in the seismic reflections of the igneous rock can be seen by the amplification of well w16 in Fig. 5. The upper surface of the igneous rocks is represented by high-amplitude reflections at ~3389 m. In between 3460 and 4023 m, the chaotic and low-amplitude reflections correspond to volcanic eruption facies igneous rocks. The strong amplitude reflections between 4023 and 4166 m are sub-volcanic facies basalts. The volcanic vent facies is observed between 4166 and 4522 m and is characterized by chaotic seismic reflections.

Seismic recognition of igneous rocks

In recent years, seismic data have been used to study igneous rocks (Hansen 2006; Jackson 2012; Magee et al. 2013a, b; Thomson 2005) using techniques such as seismic reflection characteristics, seismic volume visualization, amplitude attributes and RGB frequency decomposition (Schofield and Jolley 2013). Based on the horizon calibration and reflection analysis, we characterized four types of reflection patterns for the igneous rocks in the study area. These patterns include mushroom-shaped reflections, chimney-shaped reflections, strata-concordant reflections and funnel-shaped reflections (Fig. 6). The specific features of the four types of reflection pattern are as follows:

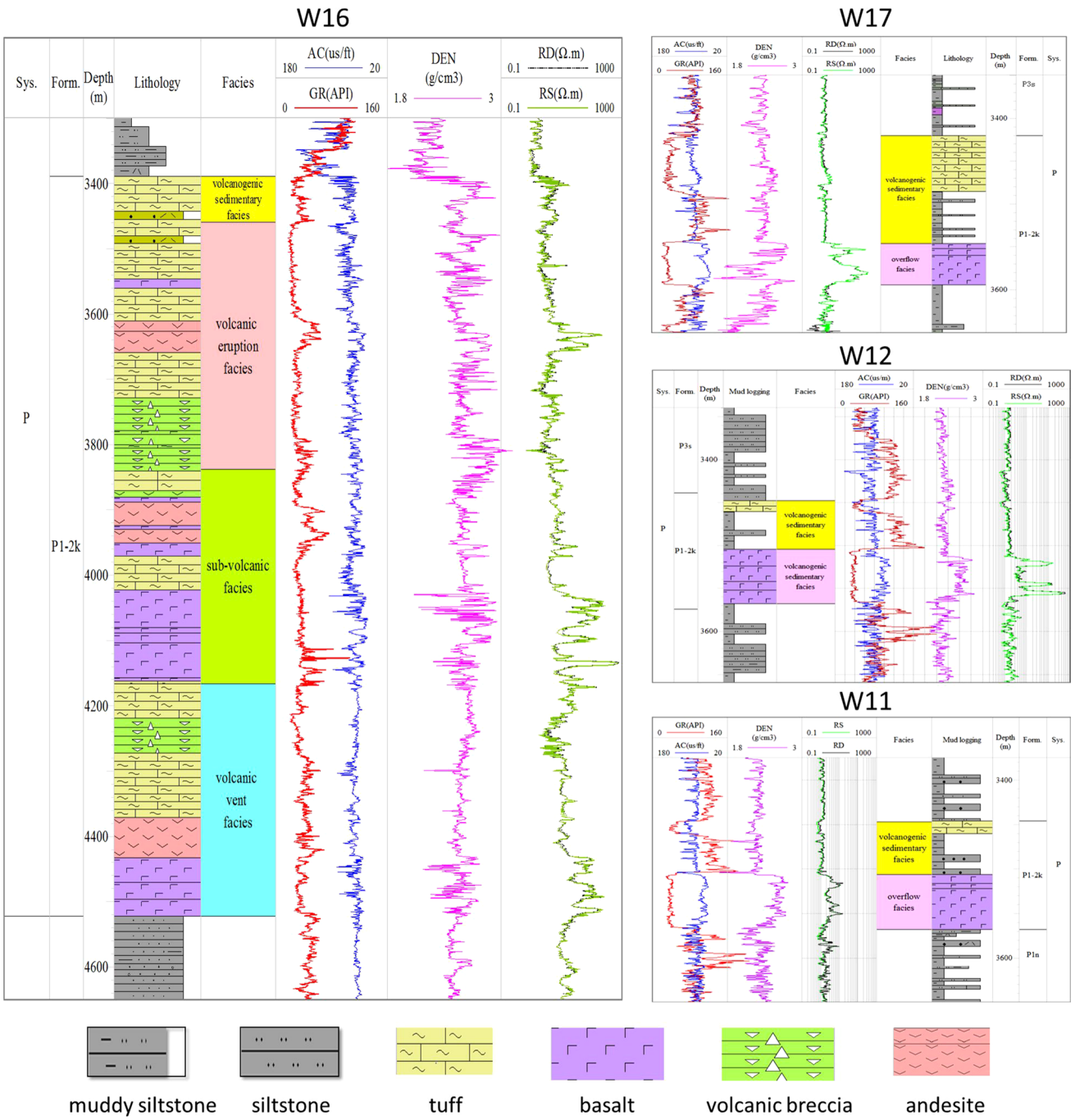

Fig. 3 Composite analysis of the four wells in the study area. *AC* acoustic, *DEN* density, *GR* gamma ray, *RD* deep investigation double lateral resistivity; *RS* shallow investigation double lateral resistivity

The mushroom-shaped reflections (Fig. 6a) have a continuous convex-upwards upper boundary with strong reflection strength. The mushroom-shaped flanks, which truncate the surrounding rocks, have medium or high amplitudes. The internal chaotic reflections exhibit a low amplitude. The bottom surface, which has medium or weak amplitude, connects with the deeper vent. The mushroom-shaped reflections form large circles in plan view (see Fig. 8a).

Well w16 penetrated the mushroom-shaped reflections. Rock cuttings retrieved from the well during drilling showed that the root of the mushroom is mostly composed of basalt, tuff and volcanic breccia. The seismic reflection is chaotic and can be assigned to the volcanic vent facies. The upper part is composed of basalt, andesite and tuff, has a high-amplitude seismic reflection and can be assigned to the sub-volcanic facies. The lower part is

Table 1 Log response characteristics of Permian lithology in study area

Lithology	GR (API)	DEN (g/cm^3)	AC (μs/ft)	RD (Ω m)
Mud	>90	<2.4	>85	<1.8
Tuff	20–67 Mean 37.6	1.9–2.5 Mean 2.35	58–101 Mean 75.6	0.5–21 Mean 2.6
Basalt	19–42 Mean 32.6	2.2–2.8 Mean 2.65	45–92 Mean 65.3	2.5–805 Mean 84.2
Andesite	35–87 Mean 52.4	2.4–2.9 Mean 2.71	55–85 Mean 62.3	2.2–314 Mean 48.6
Volcanic breccia	21–63 Mean 34.7	2.4–2.8 Mean 2.61	54–89 Mean 68.2	0.6–26 Mean 3.1

AC sonic, *DEN* density, *GR* gamma ray, *RD* deep investigate double lateral resistivity

composed of volcanic breccia, tuff and andesite, has a chaotic low-amplitude seismic reflection and can be assigned to the volcanic eruption facies. The top of the mushroom is covered by tuff interbedded with sandstone. The seismic reflection is continuous and has a strong amplitude. This part can be assigned to the volcanogenic sedimentary facies (Fig. 6a).

Chimney-shaped reflections (Fig. 6b) refer to vertically chaotic reflection belts. Volcanic cones are not observed in the upper boundaries of chimney-shaped reflections. Continuous formations become discontinuous and sometimes exhibit chaotic reflection bands. Chimney-shaped reflections feature small dots along layers (see Fig. 8a). No well was drilled directly into this feature; however, well w11 is close to this edifice, and the drilled strata include thick-bedded basalt and 14 m of tuff. We conclude that the chimney-shaped reflections are small craters.

Strata-concordant reflections (Fig. 6c) refer to laterally continuous high-amplitude reflections. The strata have attitudes that are parallel to the layering of the underlying and overlying formations. Variations in the amplitude are related to impedance differences and the thickness of the igneous rocks. Generally, the strong strata-concordant reflections lie far from the craters in plan view, and the amplitude decreases with increasing distance from the crater (Fig. 8b). The drilling results from well w12 reveal a sandwich-shaped structure. The lower part of the strata-concordant layered reflections includes 44 m of basalt, and the upper part is a >10-m-thick tuff. Between these formations are clastic rocks with a thickness of ~30 m. The

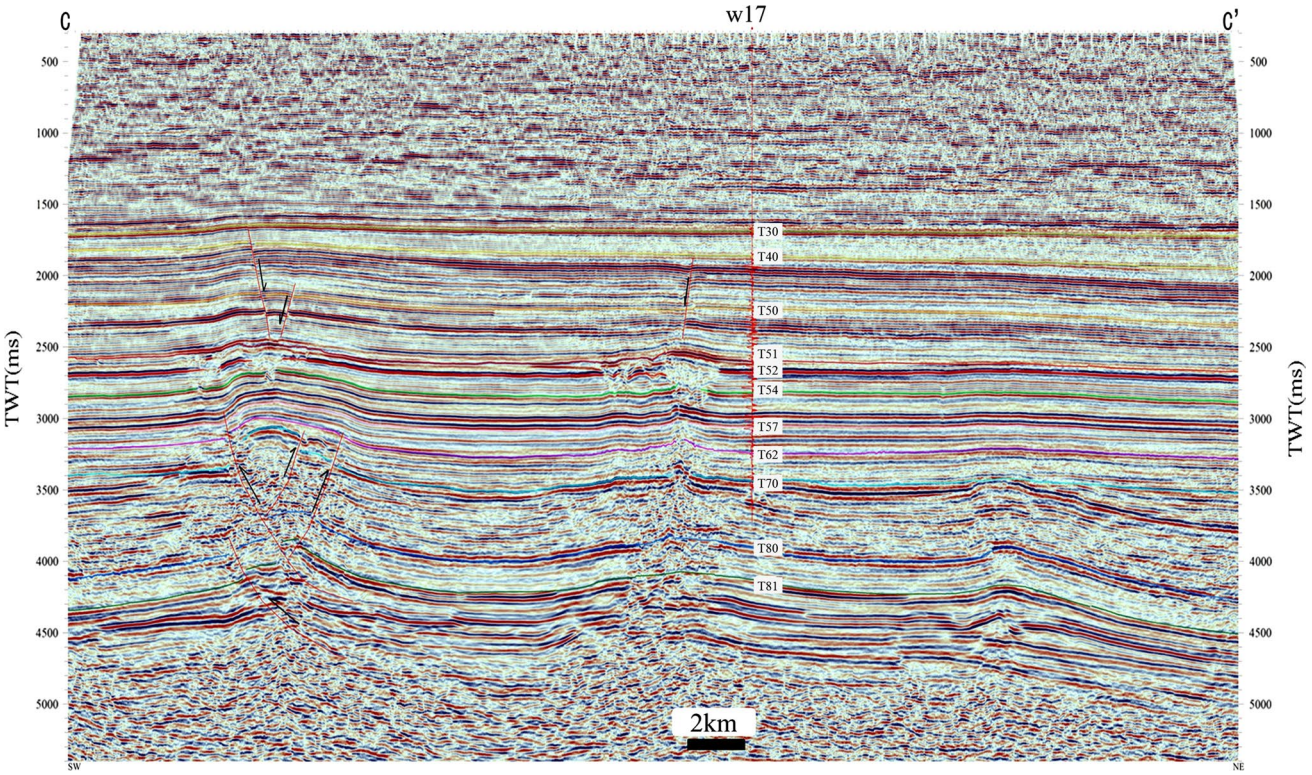

Fig. 4 Calibrated seismic section through well w17 with synthetic seismogram. The location of the profiles is indicated in Fig. 8b. *TWT* two-way travel time, *T50* bottom surface reflection of Triassic strata, *T51* top surface reflection of the Kaipaizileike formation in Permian, *T52* bottom surface reflection of the Kupukuziman formation volcanic rock in the Permian, *T54* bottom surface reflection of Permian strata, *T57* bottom surface reflection of Carboniferous strata, *T62* bottom surface reflection of mid-Silurian strata, *T70* bottom surface reflection of Silurian strata, *T80* bottom surface reflection of Ordovician strata, *T81* top surface reflection of mid-Cambrian strata

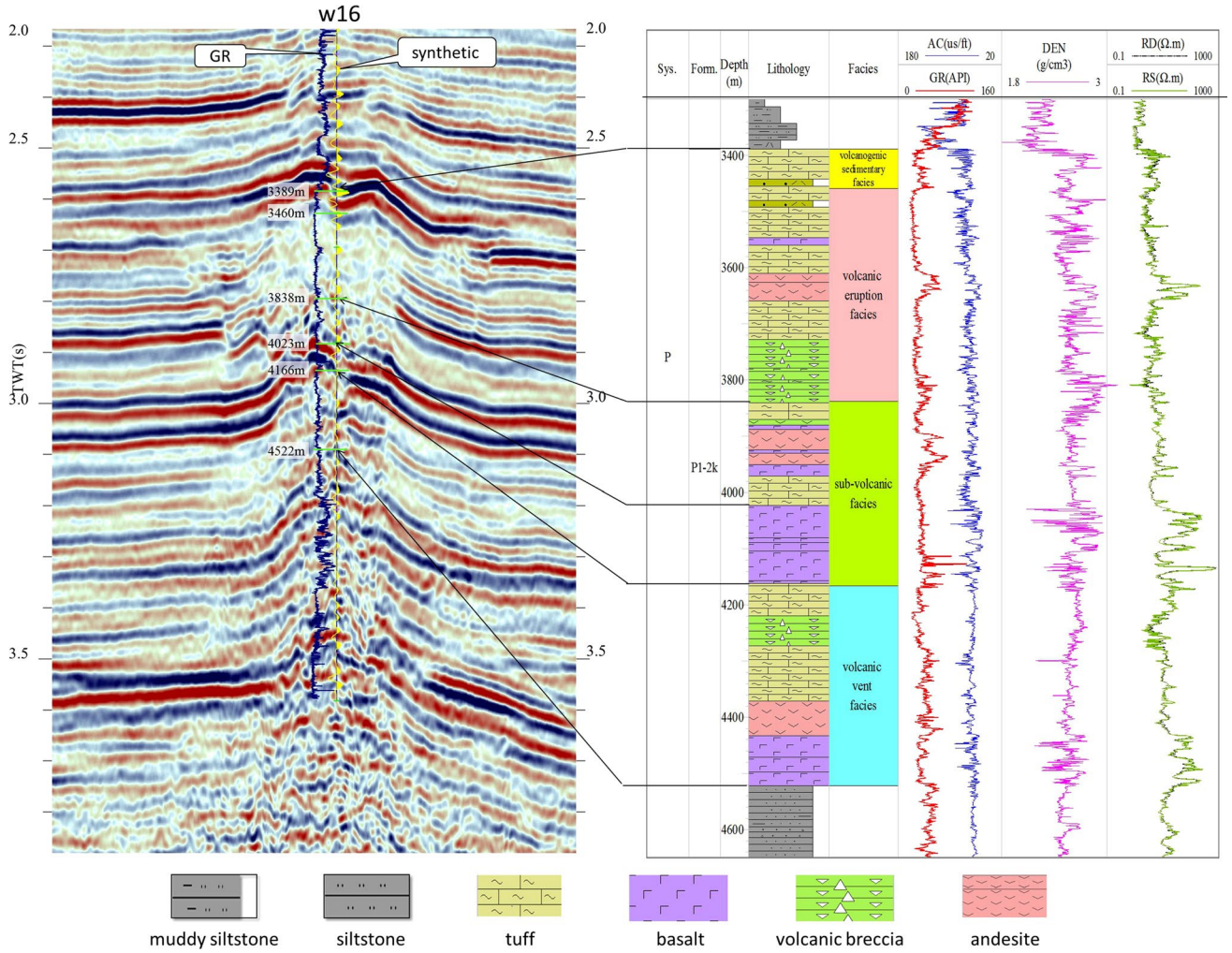

Fig. 5 Calibrated seismic section through well w16 with synthetic seismogram and the log response feature

basalts belong to the overflow facies, whereas the clastic rocks and tuff primarily belong to the volcanogenic sedimentary facies.

The funnel-shaped reflections (Fig. 6d) have a flat or concave-down upper boundary. The internal reflections of the funnel are chaotic. Normal faults are usually present in the overlying formations. In plan view, the funnel-shaped reflections form large circles or ovals (Fig. 8a) and are interpreted to be typical calderas ("Planar distribution of volcanic rocks" section).

Based on the four recognized patterns, the top and bottom of the igneous rocks and volcanic edifices were identified (Fig. 7). Most volcanic edifices in the study area are well preserved, and the main features are as follows: Multiple craters are distributed throughout the seismic profiles; beneath each volcanic cone, we observe a near-vertical volcanic vent; the formations near the vents are slightly uplifted as a result of intense magmatic activity; mushroom-shaped or approximately mushroom-shaped cones are found at the top; and normal faults cut the overlying strata. All of the volcanic edifices lie between T51 and T52 (Fig. 7).

Planar distribution of volcanic rocks

Both the craters and calderas exhibit chaotic and low-amplitude reflections inside the volcanic edifices in the seismic data, which are different from the continuous reflections generated by the surrounding formations. Considering this discrepancy, we adopted a third-generation high-precision coherency algorithm based on the eigenvalues of a covariance matrix.

In the coherency map (Fig. 8a), the dark red areas with coherency values indicate continuous wave groups in the seismic data, corresponding to stable sedimentation. The green and blue areas with high values indicate discontinuous zones, corresponding to strong lateral variations in the horizon. Several sub-circular or elliptical anomalies with high coherency values are evident in Fig. 8a, corresponding to the craters

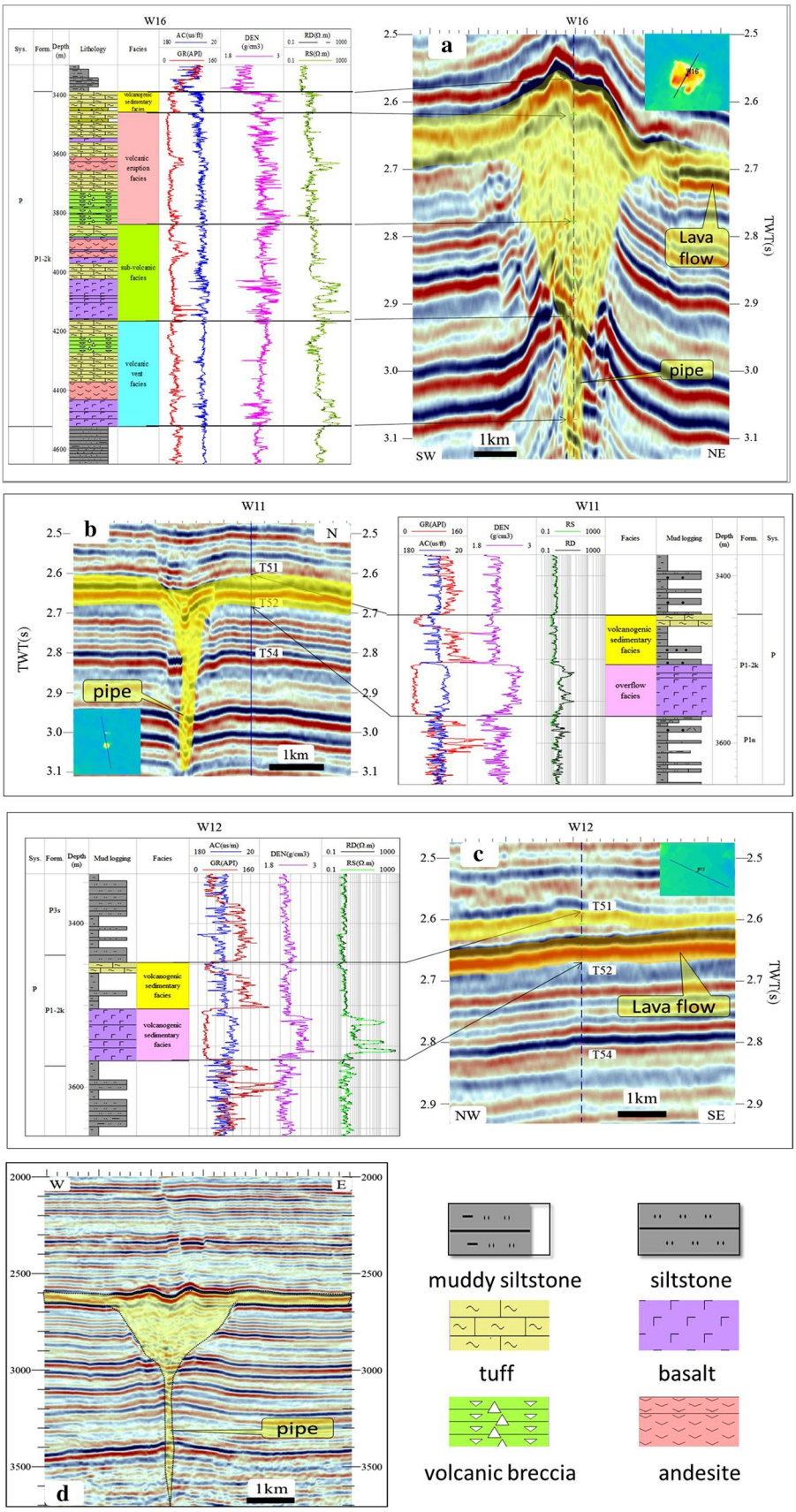

Fig. 6 Seismic reflection patterns for volcanic rocks (*yellow area* in the figure). **a** Mushroom-shaped reflections. **b** Chimney-shaped reflections. **c** Strata-concordant strong reflections. **d** Funnel-shaped reflections. *TWT* two-way travel time

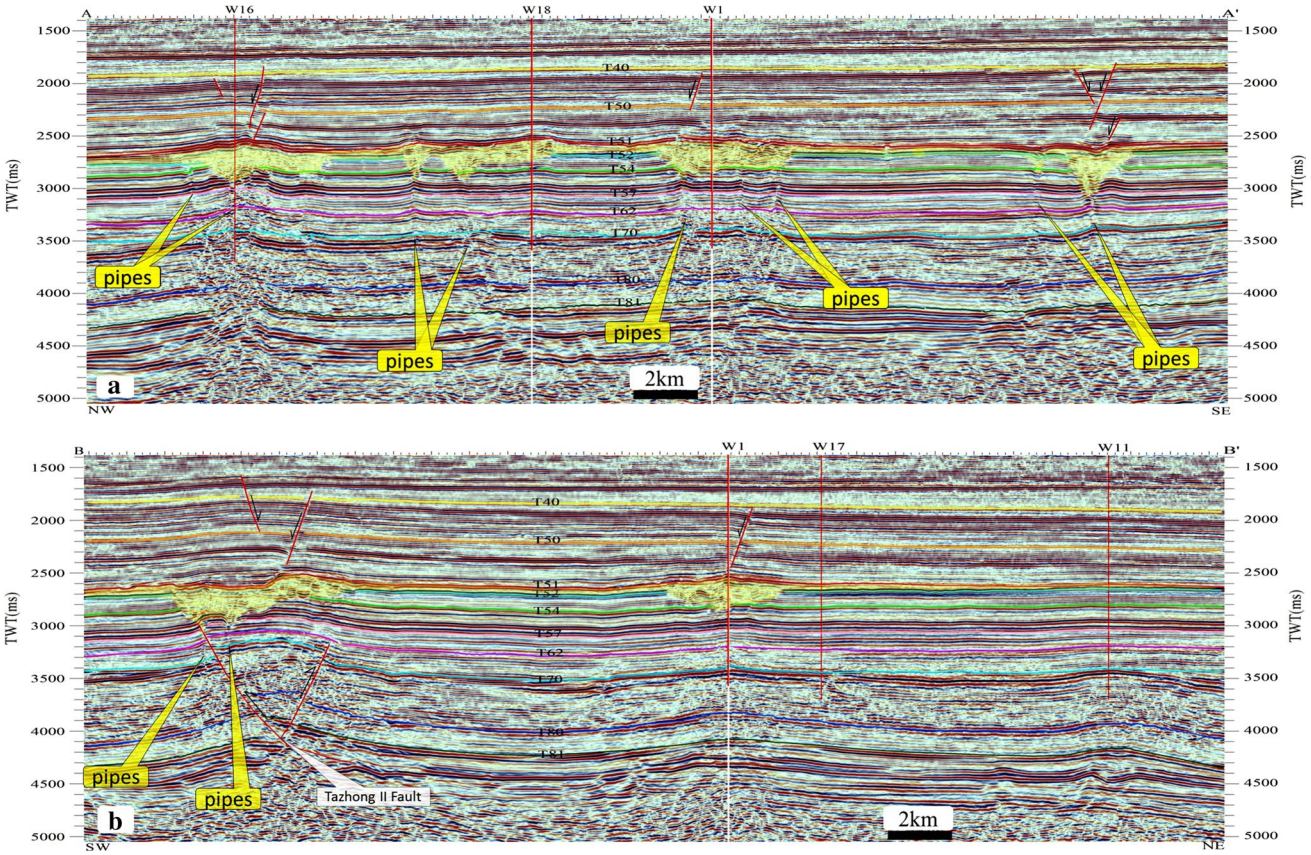

Fig. 7 **a** Section A–A' through volcanic craters (*yellow area*); **b** section B–B' through volcanic craters (*yellow area*). Locations of the two profiles are indicated in Fig. 8a. *TWT* two-way travel time

observed in the vertical seismic sections. Well w16 was drilled in the center of the volcanic craters, and wells w18 and w1 were drilled along the flanks of the volcanic edifices (Fig. 7). The two linear, high-coherency belts observed in Fig. 8a are fault zones. The WNW-trending belt in the southern part of the study area is the Tazhong II fault zone, and the NNE-trending belt in the western part is the w18 fault zone.

The edifices in the study area are large in both number and size, and the distances between the edifices are small. For convenience, we numbered the large craters with area greater than 10 km^2 from 1 to 7 in Fig. 8a. The areas of these volcanic edifices are as follows: The largest craters, 1 and 7, have areas of 43.88 and 30.54 km^2, respectively, whereas that of crater 1 is 24.47 km^2. The areas of the four other craters are between 12.47 and 15.11 km^2. The distances between the edifices are small: The nearest linear distance is 5.93 km between craters 2 and 3; and the linear distances between the other edifices are roughly around 12 km (see Fig. 8a for the exact values). There are also differences in the geometries of the edifices. For example, 1, 3, 6 and 7 are sub-circular vents; 5 is an elliptical caldera; and 2 and 4 are irregular mushroom-shaped volcanos with NNE faults.

We used RMS amplitudes to analyze the lateral distribution of the Permian igneous rocks. In Fig. 8b, high amplitudes are represented by red and yellow shading, and low amplitudes are represented by green and blue shading. Volcanic cones, which are composed of mixed volcanic debris of different sizes, generate chaotic low-amplitude reflections. The round low-amplitude anomalies in Fig. 8b represent the locations of volcanic craters, which are consistent with the coherency results (Fig. 8a). The amplitude of the top surface reflection, an indicator of thickness, decreases with decreasing thickness. In Fig. 8b, the yellow- and red-colored areas represent thicker volcanic rocks, whereas green-colored areas represent thinner volcanic rocks. The low amplitudes in the areas around well w18, which are affected by the ENE-trending faults, do not reflect the true thickness of the igneous rocks.

Thickness and volume of the igneous rocks

Thick lower Permian igneous rocks were encountered in all four wells. The thickness of the igneous rocks is 1133 m in well w16, 120 m in well w11, 152 m in well w12 and 172 m in well w17. Because the thickness of the igneous rocks in the study area exceeds the vertical resolution of the

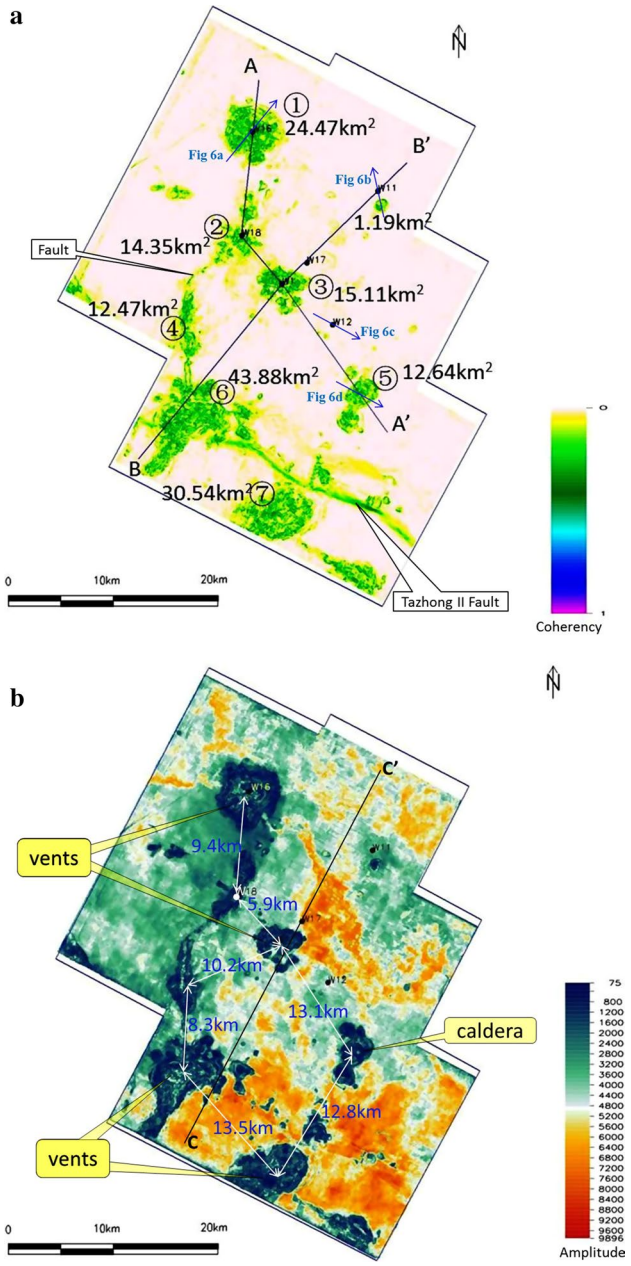

Fig. 8 Prediction maps for the distribution of igneous rocks. **a** Coherency map with time window between horizon T51 and T52. *Green-colored areas* with large coherency values indicate discontinuous seismic wave groups, corresponding to positions of volcanic craters. *Light-colored areas* with small coherency values indicate continuous seismic wave groups, corresponding to non-crater areas. **b** RMS amplitude with time window between horizon T51 and T52. *Blue-colored areas* with low amplitude indicate positions of volcanic craters. *Yellow-* and *red-colored areas* with large amplitude denote large thickness of volcanic rocks. *Green-colored areas* with medium amplitude denote small thickness of volcanic rocks. *Blue-colored areas* with small amplitude denote positions of volcanic craters

seismic data (approximately 30 m), we can directly identify and trace the top (T51) and bottom surfaces (T52) of the igneous rocks in the seismic profiles. Away from the craters, the T51 and T52 reflection surfaces are continuous, have high amplitudes and are easy to track. Because the T52 reflection surface changes greatly near the craters, we used the lower surface of the mushroom-shaped and funnel-shaped reflections to calculate the thickness (Fig. 9).

Using the TDQ module in the Landmark software, T51 and T52 were obtained in the depth domain. The thickness of the igneous rocks was calculated using the difference between T52 and T51 and a correction for the drilled thickness, resulting in a thickness map of the igneous rocks (Fig. 10). Large variations in thickness are observed, which rapidly decreases from 1100 to 300 m in the crater to several tens of meters in the northeastern part of the study area. In the central area, the thickness of the igneous rocks is greater than that in the other areas because of the overlapping eruption material from multiple craters.

Using T51 and T52 horizons of the depth domain, the structure model of the igneous rocks, which has a grid size of 25 m × 25 m (horizontal) × 10 m (vertical), was constructed using Petrel software. Based on this model, using an integral algorithm, the volume of the igneous rocks is estimated to be 178 km^3.

Discussion

Eruption patterns of the igneous rocks

Our data reveal that a central-vent eruption with multiple craters occurred in the Early Permian in the Tazhong area. According to the seismic reflection pattern, mushroom-shaped and funnel-shaped reflections are the seismic responses of volcanic edifices, and the chimney-shaped reflections are the seismic responses of volcanic vents (Figs. 6, 7). The results are supported by well data. Wells w16, w18 and w1 were drilled into different craters (Fig. 6a). Well w16 was drilled into the volcanic vent, encountering 1133 m thickness of Carboniferous to Permian volcanic rocks. Wells w18 and w1 were drilled into the flanks of the edifices, encountering 285 and 426 m of volcanic rocks, respectively. In the study area, seven large volcanic craters > 10 km^2 in area have been identified (Fig. 8a). The thickness of the volcanic rocks decreases with distance from the craters, and the thickness of the igneous rocks generally decreases from SW to NE (Fig. 10). The volcanic rock strata are relatively thin near the No. 2 fault zone in Tazhong and the ENE-trending faults in the western part. Therefore, we propose a central-vent eruption with multiple craters in the Early Permian. This conclusion differs slightly from that of a previous study in the Tarim Basin (Chen et al. 2010b), which proposed that the volcanic rocks were linearly distributed along the faults. In our study, craters were also observed in the fault zones. The collapse of the craters

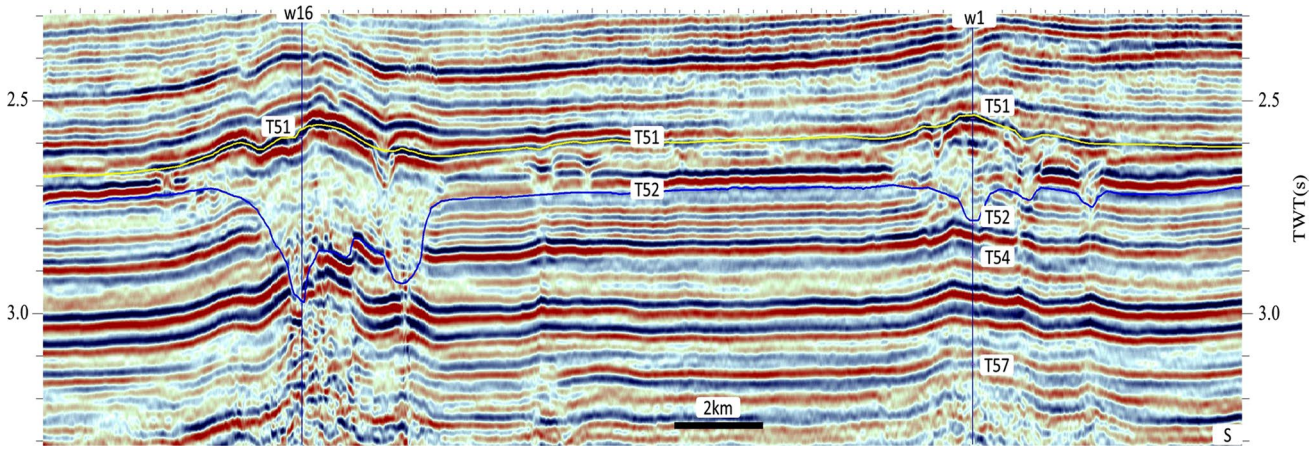

Fig. 9 Interpretation of the top and bottom surfaces of igneous rocks for thickness and volume estimation. *TWT* two-way travel time

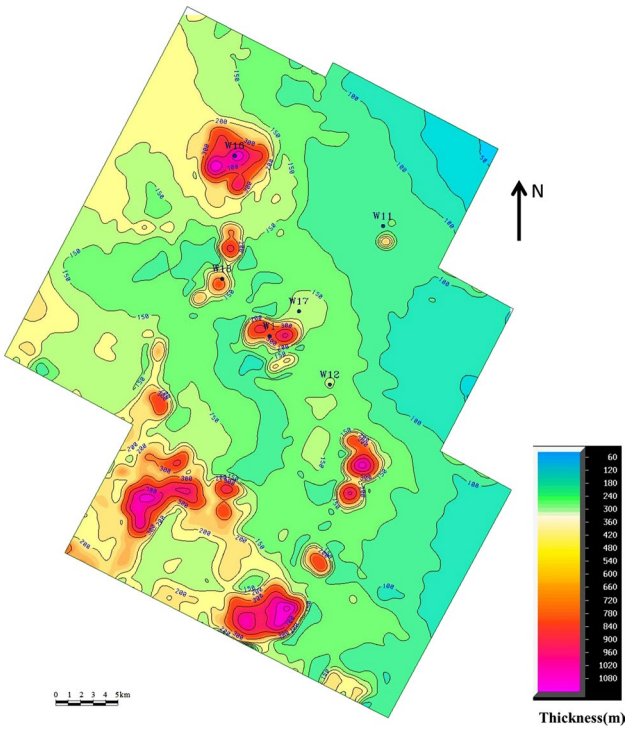

Fig. 10 Thickness of igneous rocks in the study area. In volcanic craters, the contour interval is 200 m; elsewhere the contour interval is 25 m

resulted in a flat or concave top surface in the volcanic edifices, thereby generating faults in the overlying formations. Small normal faults were found in the strata overlying the volcanic edifices (Fig. 6). The coherence analysis also indicates that the fault zones deformed the eruption instead of controlling the eruption.

Timing of the eruption of the igneous rocks

All of the recognized volcanic edifices extend from horizon T52 to T51. No crater is observed in younger formations above T51 or in older layers beneath T52. Thus, the timing of the volcanic eruptions is constrained to between the Kupukuziman and Kaipaizileike Formations, in agreement with the result of Yu et al. (2011).

The ages for the Kupukuziman and Kaipaizileike basalts are concentrated between 287 and 295 Ma (Table 2). Yu et al. (2011) obtained SHRIMP zircon U–Pb ages of 289.5 ± 2.0 Ma for the Kupukuziman basalts and 288.0 ± 2.0 Ma for the Kaipaizileike basalts in the northern Tarim Basin, which limited the duration of the entire eruption to no more than 5.5 Ma. Geochronological data have also been reported from other areas of the Tarim Basin: A K–Ar age of 289.6 ± 5.6 Ma (Li et al. 2008) and an ^{40}Ar–^{39}Ar weighted mean age of 290.1 ± 3.5 Ma (Yang et al. 2006a) were obtained from the Permian basalts exposed in the southwestern Tarim Basin; and LA-ICPMS zircon U–Pb ages of 290.9 ± 4.1 and 286.6 ± 3.3 Ma were obtained from the Permian picrite–basalt–rhyolite suite in the northern Tarim Basin.

Only one age result has been obtained from Permian basalts within the internal part of the Tarim basin. Yang et al. (1996) obtained K–Ar ages of 282.7 ± 4.1 Ma for basalts in a 3595.15 m drilling in Mancan. Our study constrains the age of the Permian igneous rocks in the internal part of the Tarim basin. Based on our data and the geochronological studies, we conclude that the thick Tarim basalts erupted during a relatively short period of time (<5 Myr) in the Early Permian (Tian et al. 2010b; Yu et al. 2011).

Table 2 Ages of Permian large igneous province in the Tarim basin

Area	Sampling location	Lithology	Age (Ma)	Method	References
Keping	Top of Kaipaizileike	Basalt	288 ± 2.0	SHRIMP	Yu et al. (2011)
	Bottom of Kupukuziman	Basalt	289.5 ± 2.0	U–Pb	
Keping	Bottom of Kaipaizileike	Basalt	295.3 ± 4.1	LA–ICP–MS	Zhang et al. (2010a)
			291.9 ± 4.5	U–Pb	
Keping	Bottom of Kupukuziman	Basalt	291.9 ± 2.2	LA–ICP–MS	Zhang et al. (2010b)
	Top of Kupukuziman	Basalt	293.9 ± 4.6	U–Pb	
Keping	Kupukuziman	Basalt	289.0 ± 6.1	K–Ar	Zhang et al. (2003)
	Kaipaizileike	Basalt	287.2 ± 5.6		
Keping	Kaipaizileike	Basalt	288.4 ± 4.4	K–Ar	Yang et al. (2005)
Keping	Kupukuziman	Basalt	292.4 ± 0.5	K–Ar	Liu and Li (1991)
Damusi	Qipan formation	Basalt	289.6 ± 5.6	K–Ar	Li et al. (2008)
Yingan	Kupukuziman	Basalt	290.1 ± 3.5	Ar–Ar	Yang et al. (2006a, b)
Yingmai	Bottom of basalt	Rhyolite	290.1 ± 3.5	LA–ICP–MS	Tian et al. (2010b)
	Top of basalt	Rhyolite	286.6 ± 3.3	U–Pb	
Mancan	Drilling 3595.15 m	Basalt	282.7 ± 4.1	K–Ar	Yang et al. (1996)

A Permian large igneous province in the Tarim Basin

In the 1445-km^2 study area, the volume of the igneous rocks is 178 km^3. The average thickness of the igneous rocks is 123 m (volume divided by area). As a conservative estimate, the volume of the entire Tarim igneous province (with an area of approximately 250,000 km^2) is 0.3 × 10^5 km^3. Four large igneous provinces are recognized in Asia: the Siberian Traps, Deccan Traps, the Emeishan large igneous province and the Tarim large igneous province (Coffin and Eldholm 1994; Xu et al. 2001; Ivanov 2007; Sheth 2007). The size of the Siberian Traps large igneous province is enormous: 7 × 10^6 km^2 in area and 4 × 10^6 km^3 in volume (Ivanov 2007). The volume of the Deccan traps is 8.2 × 10^6 km^3 (Chandrasekharam 2003). The original volume of the Emeishan large igneous province is estimated to be 0.6 × 10^6 km^3 with a rhombic area of 250,000 km^2 (Yin et al. 1992). These volumes are far greater than the estimated volume of the Tarim igneous rocks. However, the volume of the Tarim igneous rocks is a minimum estimate, for the following reasons: (1) The thicknesses of the igneous rocks in the Tarim Basin are obviously underestimated; according to Li et al. (2011) results, drill-hole data indicate that the average thickness of the Tarim Basin's igneous rocks is approximately 400–500 m, which is about four times the thickness of the volcanic rock. (2) The associated intrusives are not taken into account. (3) The volume estimated in our study is calculated using an integral algorithm. The results will be overestimated by simply multiplying the basal area by the thickness. If the second algorithm of basal area multiplied by thickness is used, the average thickness of the igneous rocks is about 500 m, and then the volume of the Tarim Basin's igneous rocks is likely greater than 0.125 × 10^6 km^3. Therefore, we suggest that the eruptive volume in the Tarim Basin was large enough to classify the region as a large igneous province.

Most geochemical data support an OIB-like mantle plume source for the Permian igneous rocks in the Tarim Basin (Yang et al. 1997; Zhang et al. 2008, 2010a, b; Zhang and Zou 2012, 2013; Zhou et al. 2004). However, the location of the plume center is still debated. The pre-volcanic lithospheric uplift is the most suitable criterion for identifying an ancient plume (Campbell and Griffiths 1990; Farnetani and Richards 1994), and the crust domal has been observed in many plume-related large igneous provinces (Williams and Gostin 2000; He et al. 2003). The center of the mantle may be the apex of the uplift (White and McKenzie 1995 and He et al. 2003). For the Emeishan large igneous province, the thickest part of the lava layer occurs in the center of the plume (Xu et al. 2001; Thompson et al. 2001; He et al. 2003, 2006). In the Tarim Basin, the thickest portions of the Permian igneous rocks are in Tazhong and NW Tarim (Yang et al. 2007). Based on the foregoing, we infer that the Tazhong area was the likely eruptive center of the mantle plume. Limited by the working area of 1445 km^2, the study area may be only part of the eruption center. The plume, which may originated from the core–mantle boundary, penetrated the overlying material, interacted with the lithosphere and finally resulted in the eruption of multiple volcanic craters in Tazhong, generating thick tuff deposits.

Conclusions

1. High-precision 3D seismic data reveal that the Permian volcanic rocks in the Tarim Basin lie between horizons T51 and T52, which correspond to the upper surface of the Kaipaizileike Formation and the lower surface

of the Kupukuziman Formation, respectively. Thus, the eruption age of the Permian volcanics is no younger than that of the Kaipaizileike Formation.

2. The seven craters of area >10 km^2 are closely spaced with the linear distances between them all being less than 13 km. The volume of magma within the 1445-km^2 study area is estimated to be 178 km^3.
3. The eruptive volume in the Tarim Basin was large enough to classify the region as a large igneous province; with the thickness portions of the Permian igneous rocks centered in the Tazhong area which was the likely eruptive center of a possible mantle plume.

Acknowledgments This work was financially supported by grants from the Natural Science Foundation of China (No. 41272211), the Northwest Oilfield Company, SINOPEC (KT2009-067) and the National S&T Major Project of China (No. 2011ZX05035-005-001HZ). Dr. Koen de Jong and an anonymous reviewer provided detailed reviews, which greatly improve this manuscript.

References

Ali JR, Thompson GM, Zhou MF, Song XY (2005) Emeishan large igneous province, SW China. Lithos 79:475–489

Benoit WR, Sethi DK, Fertl W H (1980) Geothermal well log analysis at Desert Peak, Neaada. In: SPWLA 21st annual logging symposium, Lafayette, Indiana

Brown AR (2004) Interpretation of three-dimensional seismic data, AAPG Memoir, 42, SEG Investigations in Geophysics 6th eds, 9

Campbell IH, Griffiths RW (1990) Implications of mantle plume structure for the evolution of flood basalts. Earth Planet Sci Lett 99:79–93

Chandrasekharam D (2003) Deccan fold basalts. J Geol Soc India Memoir 53:30–54

Chang H, Gong Q, Ouyang R (2003) The characteristics of igneous rocks and their influences to petroleum exploration in the center of Tarim Basin. Geophys Prospect Petroleum 42(1):49–53 **(in Chinese with English abstract)**

Chen HL, Yang SF, Dong CW, Zhu GQ, Jia CZ, Wang ZG (1997a) Research on geological thermal events of Tarim basin. Chin Sci Bull 42(10):1096–1099 **(in Chinese with English abstract)**

Chen HL, Yang SF, Dong CW, Jia CZ, Wei GQ, Wang ZG (1997b) Confirmation of Permian basite zone in Tarim basin and its tectonic significance. Geochimica 26(6):77–87 **(in Chinese with English abstract)**

Chen HL, Yang SF, Wang QH, Luo JC, Jia CZ, Wei GQ, Li ZL, He GY, Hu AP (2006) Sedimentary response to the Early-Mid Permian basaltic magmatism in the Tarim plate. Geol China 33:545–552 **(in Chinese with English abstract)**

Chen TJ, Cui RF, Xu YZ, Wang X (2009) Method to locate igneous rock intrusion of coal bed using P-wave Data. Proced Earth Planet Sci 1:963–969

Chen MM, Tian W, Zhang ZL, Pan WQ, Song Y (2010a) Geochronology of the Permian basic- intermediate- acidic magma suite from Tarim, Northwest China and its geological implications. Acta Petrol Sinica 26(2):559–570 **(in Chinese with English abstract)**

Chen X, Dong YW, Hao GL (2010b) Magmatic activities and their influences on hydrocarbon accumulation in the early Permian, Central Tarim Basin. Geol Sci Technol Inf 29(5):78–83 **(in Chinese with English abstract)**

Coffin MF, Eldholm O (1994) Large igneous provinces: crustal structure, dimensions, and external consequences. Rev Geophys 32:1–36

Davies RJ, Bell BR, Cartwright JA, Shoulders S (2002) Three-dimensional seismic imaging of Palaeocene dike-fed submarine volcanoes from the northeast Atlantic margin. Geology 30:223–226

Du JH, Zhou XY, Li QM, Wu GH, Pan WQ, Yang T (2011) Characteristics and controlling factors of the large carbonate petroleum province in the Tarim Basin, NW China. Petrol Explor Dev 38(6):652–661

Farnetani CG, Richards MA (1994) Numerical investigation of the mantle plume initiation model for flood basalt events. J Geophys Res 99:813–833

Ge RF, Zhu WB, Zheng BH, Wu HL, He JW, Zhu XQ (2012) Early Pan-African magmatism in the Tarim Craton: insights from zircon U–Pb–Lu–Hf isotope and geochemistry of granitoids in the Korla area, NW China. Precambr Res 212–213:117–138

Gersztenkorna, Marfurtk J (1999) Eigenstructure based coherence computations as an aid to 3-D structural and stratigraphic mapping. Geophysics 64(5):1468–1479

Hansen DM (2006) The morphology of intrusion-related vent structures and their implications for constraining the timing of intrusive events along the NE Atlantic margin. J Geol Soc 163:789–800

He B, Xu YG, Chung SL, Xiao L, Wang YM (2003) Sedimentary evidence for a rapid, kilometer-scale crustal doming prior to the eruption of the Emeishan flood basalts. Earth Planet Sci Lett 213:391–405

He DF, Jia CZ, Li DS, Zhang CJ, Meng QR, Shi X (2005) Formation and evolution of polycyclic superimposed Tarim Basin. Oil Gas Geol 26(1):64–77

He B, Xu YG, Wang YM, Luo ZY (2006) Sedimentation and lithofacies paleogeography in southwestern China before and after the emeishan flood volcanism: new insights into surface response to mantel plume activity. J Geol 114:117–132

Ivanov AV (2007) Evaluation of different models for the origin of the Siberian Traps. In: Foulger GR, Jurdy DM (eds) Plumes and planetary processes: Geological Society of America Special Paper, 430, pp 669–691

Jackson CAL (2012) Seismic reflection imaging and controls on the preservation of ancient sill-fed magmatic vents. J Geol Soc London 169:503–506

Jia CZ (1997) Tectonic characteristics and oil-gas, Tarim Basin. Petroleum Industry Press, Beijing **(in Chinese)**

Kang YZ, Kang ZH (1996) Tectonic evolution and oil and gas of Tarim basin. J SE Asian Earth Sci 13(35):317–325

Li S, Wang T (1980) Volcanic rocks. Beijing Geological Publishing House, pp 20–40 (**in Chinese**)

Li ZL, Yang SF, Chen HL, Langmuir HC, Yu X, Lin XB, Lin YQ (2008) Chronology and geochemistry of Taxinan basalts from the Tarim basin: evidence for Permian plume magmatism. Acta Petrol Sinica 24:959–970 **(in Chinese with English abstract)**

Li N, Qiao DX, Li QF, Wu HL, Fu YS, Dong LX, Feng QF, Wang KW (2009) Theory on logging interpretation of igneous rocks and its Application. Petrol Explor Dev 36(6):683–692

Li ZL, Chen HL, Song B, Li YQ, Yang SF, Yu X (2011) Temporal evolution of the Permian large igneous province in Tarim Basin in northwestern China. J Asian Earth Sci 42:917–927

Li ZL, Li YQ, Chen HL, Santosh M, Yang SF, Xu YG, Charles HL, Chen ZX, Zou SY (2012a) Hf isotopic characteristics of the Tarim Permian large igneous province rocks of NW China: implication for the magmatic source and evolution. J Asian Earth Sci 49:191–201

Li YQ, Li ZL, Sun YL, Santosh M, Charles HL, Chen HL, Yang SF, Chen ZX, Yu X (2012b) Platinum-group elements and

geochemical characteristics of the Permian continental flood basalts in the Tarim Basin, northwest China: implications for the evolution of the Tarim Large Igneous Province. Chem Geol 328:278–289

Li CX, Wang XF, Li BL, He DF (2013) Paleozoic fault systems of the Tazhong Uplift, Tarim Basin, China. Mar Pet Geol 39:48–58

Liu JQ, Li WM (1991) Petrological characteristics and ages of basalt in North Tarim. In: Jia RX (ed) Research of petroleum geology of Northern Tarim Basin in China, stratigraphy and sedimentology, vol I. Chinese University of Geoscience Press, Beijing, pp 194–201 **(in Chinese with English abstract)**

Liu X, Guan P, Pan WQ, Tian W, Huang SY, Pan Y, Jing B, Yu HJ (2011) Meticulous characterization of permian volcanic rocks' spatial distribution and its geological significance in the Tarim Basin. Acta Sci Nat Univ Pekin 47(2):315–320 **(in Chinese with English abstract)**

Lu SN, Li HK, Zhang CL, Niu GH (2008a) Geological and geochronological evidences for the Precambrian evolution of the Tarim Craton and surrounding continental fragments. Precambr Res 160:94–107

Lu XX, Bai ZK, Zhao FY (2008b) Hydrocarbon accumulation and distribution characteristics of the silurian in the Tazhong Uplift of Tarim Basin. Earth Sci Frontiers 156–166

Magee C, Esther HS, Christopher ALJ (2013a) Volcano growth mechanisms and the role of sub-volcanic intrusions: Insights from 2D seismic reflection data. Earth Planet Sci Lett 373:41–53

Magee C, Jackson CAL, Schofield N (2013b) The influence of normal fault geometry on igneous sill emplacement and morphology. Geology 41:407–410

Pan Y, Jiang ZG, Pan M, Tian W, Qi XZ (2008) Method for identifying igneous lithological in the west of Northern Tarim Basin. J Oil Gas Technol 30(1):260–262 **(in Chinese with English abstract)**

Pirajno F, Ernst RE, Borisenko AS, Fedoseev G, Naumov EA (2009) Intraplate magmatism in Central Asia and China and associated metallogeny. Ore Geol Rev 35:114–136

Sanyal SK, Mathews MA (1979) Matrix and response characteristics for sonic, density, and neutron. In: SPWLA 20th annual logging symposium, Tulsa

Schofield N, Jolley DW (2013) Development of intra-basaltic lava-field drainage systems within the Faroe-Shetland Basin. Petrol Geosci 19:273–288

Shangguan SM, Tian W, Xu YG, Guan P, Pan L (2012) The eruption characteristics of the Tarim flood basalt. Acta Petrol Sinica 28(4):1261–1272 **(in Chinese with English abstract)**

Sheth HC (2007) Plume-related regional pre-volcanic uplift in the Deccan Traps: absence of evidence, evidence of absence. In: Foulger GR, JurdyDM (eds) Plates, plumes, and planetary processes: Geological Society of America Special Paper 430, pp 785–813. doi:10.1130/2007.2430(36)

Shu LS, Deng XL, Zhu WB, Ma DS, Xiao WJ (2011) Precambrian tectonic evolution of the Tarim Block, NW China: new geochronological insights from the Quruqtagh domain. J Asian Earth Sci 42:774–790

Sun DS, Ling Y, Guo XY, Gao J, Lin JX (2010) Application of discrete frequency coherence cubes in the fracture detection of volcanic rocks in full-azimuth seismic data. In: SEG Denver 2010 annual meeting, pp 1342–1346

Thompson GM, Ali JR, Song XY, Jolley DW (2001) Emeishan basalts, southwest China: reappraisal of the formation's type area stratigraphy and a discussion of its significance as a large igneous province. J Geol Soc Lond 158:593–599

Thomson K (2005) Volcanic features of the North Rockall Trough: application of visualisation techniques on 3D seismic reflection data. Bull Volcanol 67:116–128. doi:10.1007/s00445-004-0363-9

Tian H, Xiao XM, Ronald WT, Wilkins Gan HJ, Guo LG, Yang LG (2010a) Genetic origins of marine gases in the Tazhong area of the Tarim basin, NW China: implications from the pyrolysis of marine kerogens and crude oil. Int J Coal Geol 82:17–26

Tian W, Campbell IH, Allen C, Guan P, Pan W, Chen M, Yu H, Zhu W (2010b) The Tarim picrite-basalt-rhyolite suite-a Permian flood basalt from northwest China with contrasting rhyolites produced by fractional crystallization and anatexis. Contrib Miner Petrol 60(3):407–425

Wagner-Friedrichs M, Krastel S, Spiess V, Ivanov M, Bohrmann G, Meisner L (2008) Three-dimensional seismic investigations of the Sevastopol mud volcano in correlation to gas/fluid migration pathways and indications for gas hydrate occurrences in the Sorokin Trough (Black Sea). Geochem Geophys Geosyst 9:Q05012. doi:10.1029/2007GC001685

Wang PJ, Chi YL, Liu WZ, Cheng RH (2003) Volcanic facies of the Song Liao Basin: classification characteristics and reservoir significance. J Jilin Univ (Earth Sci Edn) 33(4):449–454

Wang BZ, Xu LM, Wang SX (2006) Prediction for igneous intrusive mass of clastic reservoir in the pericline area around central Tarim Basin. Geophys Prospect Petrol 45(6):602–606 **(in Chinese with English abstract)**

Wang BQ, Huang ZB, Ma PL, Pan ZZ, Wang LL (2009) Establishment of division standard, evidence and principle of structural units in Tarim Basin. Geot Metal 33:86–93 **(in Chinese with English abstract)**

White R, McKenzie D (1995) Mantle plumes and flood basalts. J Geophys Res 100:17543–17585

Williams GE and Gostin VA (2000) Mantle plume uplift in the sedimentary record: origin of kilometre-deep canyons within late Neoproterozoic successions. S Aust J Geol Soc 157:759–768

Wright KA, Davies RJ, Jerram DA, Morris J, Fletcher R (2012) Application of seismic and sequence stratigraphic concepts to a lave-fed delta system in the Faroe-Shetland Basin. UK and Faroes. Basin Res 24:91–106. doi:10.1111/j.1365-2117.2011.00513.x

Xiao XM, Song ZG, Liu DH, Liu ZF, Fu JM (2000) The Tazhong hybrid petroleum system, Tarim Basin, China. Mar Pet Geol 17:1–12

Xu YG, Chung SL, Jahn BM, Wu GY (2001) Petrologic and geochemical constraints on the petrogenesis of Permian-Triassic Emeishan flood basalts in southwestern China. Lithos 58:145–168

Xu YG, He B, Chung SL, Menzies MA, Frey FA (2004) Geologic, geochemical, and gophysical consequences of plume involvement in the Emeishan flood-basalt province. Geology 32:917–920

Xu YG, He B, Huang XL, Luo ZY, Chung SL, Xiao L, Zhu D, Shao H, Fan WM, Xu JF, Wang YJ (2007) Identification of mantle plumes in the Emeishan Large Igneous Province. Episodes 30:32–42

Xu YZ, Yang HJ, Liu YF, Wang SS, Yang P, Zhao JX (2012) Application of seismic facies and attributes analysis on the identification of Permian igneous rock. Int J Min Sci Technol 22:471–475

Yan L, Li M, Pan WQ (2014) Distribution characteristics of Permian igneous rock in Tarim Basin-based on the high-precision aeromagnetic data. Progr Geophys 29(4):1843–1848 **(in Chinese with English abstract)**

Yang SF, Chen HL, Dong CW, Jia CZ, Wei GQ, Wang ZG (1996) The discovery of Permian syenite inside Tarim basin and its geodynamic significance. Geochemica 25:121–128 **(in Chinese with English abstract)**

Yang SF, Chen HL, Dong CW, Jia CZ, Wei GQ, Wang ZG (1997) Geological thermal event of Tarim basin. Chin Sci Bull 42:1096–1099 **(in Chinese with English abstract)**

Yang SF, Chen HL, Ji DW, Li ZL, Dong CW (2005) Geological process of early to middle Permian magmatism in Tarim Basin and its geodynamic significance. Geol J China Univ 11(4):504–511 **(in Chinese with English abstract)**

Yang SF, Li ZL, Chen HL, Chen W, Yu X (2006a) ^{40}Ar–^{39}Ar dating of basalts from Tarim Basin, NW China and its implication to a Permian thermal tectonic event. J Zhejiang Univ Sci (Supp. II) 7:170–174

Yang SF, Li ZL, Chen HL, Xiao WJ, Lin XB, Shi XG (2006b) Discovery of a Permian quartz syenitic porphyritic dyke from the Tarim Basin and its tectonic implications. Acta Petrol Sinica 22:1405–1412

Yang SF, Li Z, Chen HL, Santosh M, Dong CW, Yu X (2007) Permian bimodal dyke of Tarim Basin, NW China: geochemical characteristics and tectonic implications. Gondwana Res 12:113–120

Yang H, Xu HM, Huang Y, Sun P, Niu YJ, Liu H (2013) Identification of magmatic rocks and their hydrocarbon accumulation significance in the Central Tarim. Chin Technol Rev 31(1):38–42

Yin HF, Huang S, Zhang K, Hansen HJ, Yang FQ, Ding M, Bie X (1992) The effects of volcanism on the Permo-Triassic mass extinction in South China. In: Sweet WC (ed) Permo-Triassic Events in the Eastern Tethys. Cambridge University Press, Cambridge, pp 146–157

Yu X, Yang SF, Chen HL, Chen ZQ, Li ZL (2011) Permian flood basalts from the Tarim Basin, Northwest China: SHRIMP zircon U-Pb dating and geochemical characteristics. Gondwana Res 20:485–497

Zhang CL (2003) Identification and prediction of volcanic bodies in Tazhong area of the Tarim Basin. Petrol Geol Exp 25(5):513–516 **(in Chinese with English abstract)**

Zhang CL, Zou HB (2012) Comparison between the Permian mafic dykes in Tarim and the western part of Central Asian Orogenic Belt (CAOB), NW China: implications for two mantle domains of the Permian Tarim Large Igneous Province. Lithos. doi:10.1016/j.lithos.2012.11.010

Zhang CL, Zou HB (2013) Permian A-type granites in Tarim and western part of Central Asian Orogenic Belt (CAOB): genetically related to a common Permian mantle plume? Lithos. doi:10.1016/j.lithos.2013.04.001

Zhang SB, Ni YN, Gong FH (2003) A guide to the stratigraphic investigation on the Periphery of the Tarim Basin. Petroleum Industry Press, Beijing (**in Chinese**)

Zhang CL, Li XH, Li ZX, Ye HM, Li CN (2008) A Permian layered intrusive complex in the western Tarim Block, northwestern China: product of a ca.275 Ma mantle plume? J Geol 116:112–128

Zhang CJ, Jia CZ, Li BL, Luo XY, Liu YX (2010a) Ancient karsts and hydrocarbon accumulation in the middle and western parts of the North Tarim uplift, NW China. Petrol Explor Dev 37(3):263–269

Zhang CL, Xu YG, Li ZX, Wang HY, Ye HM (2010b) Diverse Permian magmatism in the Tarim Block, NW China: genetically linked to the Permian Tarim mantle plume? Lithos 119:537–552

Zhang YT, Liu JQ, Guo ZF (2010c) Permian basaltic rocks in the Tarim basin, NW China: implications for plume–lithosphere interaction. Gondwana Res 18:596–610

Zhang DY, Zhou TF, Yuan F, Simon MJ, Fan Y, Liu S (2012) Source, evolution and emplacement of Permian Tarim Basalts: evidence from U–Pb dating, Sr–Nd–Pb–Hf isotope systematics and whole rock geochemistry of basalts from the Keping area, Xinjiang Uygur Autonomous region, northwest China. J Asian Earth Sci 49:175–190

Zhang DY, Zhang ZC, Santosh M, Cheng ZG, Huang H, Kang JL (2013) Perovskite and baddeleyite from kimberlitic intrusions in the Tarim large igneous province signal the onset of an end-Carboniferous mantle plume. Earth Planet Sci Lett 361:238–248

Zhao WZ, Zou CN, Feng ZQ, Hu SY (2008) Geological features and evaluation techniques of deepseated volcanics gas reservoirs, Songliao Basin. Petrol Explor Dev 35(2):129–142

Zheng LD, Yang ZY, Tong YB, Yuan W (2010) Magnetostratigraphic constraints on two-stage eruptions of the Emeishan continental flood basalts. Geochem Geophys Geosyst 11(12):1525–2027

Zhou MF, Lesher CM, Yang ZX, Li JW, Sun M (2004) Geochemistry and petrogenesis of 270 Ma Ni-Cu-(PGE) sulfide-bearing mafic intrusions in the Huangshan district; Eastern Xinjiang; Northwest China: implications for the tectonic evolution of the Central Asian orogenic belt. Chem Geol 209:233–257

Zhou MF, Zhao JH, Jiang CY, Gao JF, Wang W, Yang SH (2009) OIB-like, heterogeneous mantle sources of Permian basaltic magmatism in the western Tarim Basin, NW China: implications for a possible Permian large igneous province. Lithos 113:583–594

Zhou XY, Pang XQ, Li QM, Pang H, Xiang CF, Jiang ZX, Li SM, Liu LF (2010) Advances and problems in hydrocarbon exploration in the Tazhong area, Tarim Basin. Pet Sci 7:164–178

Zhu YX, Jin ZJ, Lin CS, Lu XX, Xie QL (2005) Relations between the early Permian magmatic rocks and hydrocarbon accumulation in the central Tarim. Petrol Geol Exp 27(1):50–54 **(in Chinese with English abstract)**